4-8-2021

Diagnosing Non-Gaussian Temperature Distribution Tails Using Back-Trajectory Analysis

A. J. Catalano
Portland State University

P. C. Loikith
Portland State University, ploikith@pdx.edu

J. D. Neelin
University of California, Los Angeles

Citation Details

Catalano, A. J., Loikith, P. C., & Neelin, J. D. (2021). Diagnosing Non-Gaussian Temperature Distribution Tails Using Back-Trajectory Analysis. *Journal of Geophysical Research: Atmospheres*, *126*(8). https://doi.org/10.1029/2020jd033726

JGR Atmospheres

RESEARCH ARTICLE
10.1029/2020JD033726

Diagnosing Non-Gaussian Temperature Distribution Tails Using Back-Trajectory Analysis

A. J. Catalano[1], P. C. Loikith[1], and J. D. Neelin[2]

[1]Department of Geography, Portland State University, Portland, OR, USA, [2]Department of Atmospheric and Oceanic Sciences, University of California, Los Angeles, CA, USA

Key Points:

- Air parcel back trajectories help to explain the pathways for non-Gaussian temperature distribution tails at select extratropical locations
- Extreme temperatures in locations with non-Gaussian temperature distribution tails can occur with a range of meteorological mechanisms
- Tail non-Gaussianity is governed by the proximity of the location to influential geography and climatologically anomalous air source regions

Supporting Information:

Supporting Information may be found in the online version of this article.

Correspondence to:

P. C. Loikith,
ploikith@pdx.edu

Citation:

Catalano, A. J., Loikith, P. C., & Neelin, J. D. (2021). Diagnosing non-Gaussian temperature distribution tails using back-trajectory analysis. *Journal of Geophysical Research: Atmospheres*, *126*, e2020JD033726. https://doi.org/10.1029/2020JD033726

Received 17 AUG 2020
Accepted 31 MAR 2021

Author Contributions:

Conceptualization: A. J. Catalano, P. C. Loikith, J. D. Neelin
Data curation: A. J. Catalano
Formal analysis: A. J. Catalano
Funding acquisition: P. C. Loikith, J. D. Neelin
Investigation: A. J. Catalano
Methodology: A. J. Catalano, P. C. Loikith, J. D. Neelin
Software: A. J. Catalano
Supervision: P. C. Loikith, J. D. Neelin
Validation: A. J. Catalano, P. C. Loikith
Visualization: A. J. Catalano
Writing – original draft: A. J. Catalano
Writing – review & editing: A. J. Catalano, P. C. Loikith, J. D. Neelin

Abstract Coherent regions exhibiting non-Gaussian 2-m temperature distribution tails are present across the globe, indicating changes in extreme temperatures under future warming may manifest in more complex ways than were the underlying distributions symmetric about the mean. To further the understanding of physical processes that govern temperature distribution tail shape, this work utilizes a back-trajectory model to diagnose mechanisms for extreme daily mean temperature development at select extratropical locations exhibiting non-Gaussian tails. Although characteristics such as direction, distance, and temperature evolution vary among back-trajectories associated with extreme temperature days, results reveal principal pathways for air parcel propagation associated with preferred patterns in large-scale circulation. A relatively persistent synoptic setup leads to thermal advection, which interacts with local geographic features to produce a shorter- or longer-than-Gaussian tail. Significant relationships with recurrent modes of atmospheric and sea surface temperature variability further suggest the influence of teleconnection wave patterns and ocean temperatures on extreme daily temperature occurrence over land, though local, smaller-scale processes are also important. Air parcels transporting extreme temperatures at short-tailed locations often originate in marine environments, constraining the magnitude of the temperature extreme, while locations exhibiting long cold tails require rare meteorological conditions to transport the coldest air from poleward source regions often partially blocked by topography or downstream of the prevailing wind. Processes governing longer-than-Gaussian warm tails at locations examined are more subtle and not as obviously dominated by horizontal advection. Results provide added insight into our understanding of temperature extremes and how they may change in the future at regional scales.

1. Introduction

Anthropogenic warming has intensified drought conditions (Lehner et al., 2006), reduced frost day occurrence (Easterling, 2002), and altered ecosystems (Walther et al., 2002). Although continued and projected warming broadly increases warm and decreases cold extremes (Kharin et al., 2013), these changes will not occur at a uniform rate globally. For example, some regions have experienced changes in seasonal temperature extremes in excess of changes in the mean, including winter warm extremes in Europe (Gross et al., 2019). Previous work showed this region exhibits a shorter-than-Gaussian temperature distribution warm tail, meaning it would experience a more-rapid-than-Gaussian increase in exceedance frequency of a fixed extreme temperature threshold under a uniform warm shift, consistent with climate model projections (Loikith et al., 2018).

The prevalence of non-Gaussian near-surface temperature distributions is well-documented (Cavanaugh & Shen, 2014; Perron & Sura, 2013). Recent work has investigated how large-scale dynamics within a background meridional temperature gradient produces large, spatially coherent regions of asymmetrical temperature distributions. For example, atmospheric stirring generated by Rossby wave propagation plays a role in mid-latitude distribution asymmetry (Garfinkel & Harnik, 2017; Linz et al., 2018). Tamarin-Brodsky et al. (2019) also highlighted the role of temperature advection in governing distribution skewness using a Lagrangian feature-tracking technique, with implications for changes in extreme temperatures under global warming (Tamarin-Brodsky et al., 2020).

Identifying the fundamental dynamics governing broad temperature distribution symmetry is valuable for determining how extreme temperatures may change in a warming climate. However, non-Gaussian

temperature distribution tails are also governed by local-to-regional processes and geography. Synoptic-scale meteorological patterns are key drivers of physical processes, such as advection, that lead to local extreme temperature development. Pfahl (2014) determined that anomalous blocking to the north and cyclonic circulation to the southeast contribute to easterly advection of cold extremes over Europe, whereas warm extremes in western North America are generally associated with a strong ridge and upstream trough (Grotjahn et al., 2016). Preferred patterns of synoptic circulation suggest the influence of recurrent modes of climate variability on temperature extremes (e.g., Loikith & Broccoli, 2014; Thompson & Wallace, 2001). The interaction between circulation and local topography is also important to extreme temperature development (Loikith & Broccoli, 2012) and can lead to non-Gaussianity in the distribution tail. Using a mechanistic approach, Loikith and Neelin (2019) revealed the influence of both synoptic-scale circulation and proximate geographic features such as mountainous terrain and bodies of water on cold-tail non-Gaussianity. To enhance understanding of the range of current-climate determinants specific to non-Gaussian temperature distribution tails, this work builds upon Loikith and Neelin (2019) by examining back-trajectories and their upstream environment to identify the range of pathways leading to extreme temperature development, and the processes contributing to a selection of shorter- and longer-than-Gaussian distribution tails.

2. Data

Meteorological data are obtained from the latest European Centre for Medium-Range Weather Forecasts reanalysis, ERA5 (Hersbach et al., 2020), which provides hourly data at a 31-km horizontal resolution and 137 vertical levels. To analyze relationships between extreme temperatures and modes of atmospheric variability, daily Pacific-North American pattern (Wallace & Gutzler, 1981), Northern Annular Mode (Thompson & Wallace, 2001), North Atlantic Oscillation (Hurrell, 1995), and Southern Annular Mode (Limpasuvan & Hartmann, 1999) indices are obtained from the NOAA Climate Prediction Center. For relationships with sea surface temperature variability, monthly El Niño-Southern Oscillation (ENSO; Horel & Wallace, 1981) indices are obtained from the KNMI Climate Explorer, Pacific Decadal Oscillation (Mantua et al., 1997) indices are obtained from JISAO at University of Washington, and Indian Ocean Dipole (Saji et al., 1999) indices are obtained from the NOAA ESRL Physical Sciences Laboratory.

3. Methodology

3.1. Non-Gaussian Tail Identification

Analyses are performed over the period 1980–2014 for two meteorological seasons: December, January, and February (DJF) and June, July, and August (JJA). Two-meter temperature anomalies are computed by subtracting the daily climatology from each day. Then, the linear trend for each season is removed. Following Loikith and Neelin (2015), a shift ratio approach is utilized to determine locations with 2-m temperature anomaly distribution tails departing significantly from Gaussian. This process is briefly outlined below:

- At each grid cell, extreme temperatures in cold and warm tails of the reference temperature anomaly distribution are identified as values beyond the 5th and 95th percentile thresholds, respectively
- Distributions are shifted to the right by 0.5 standard deviations (σ; defined as the standard deviation of the ERA5 daily temperature anomaly distribution at that grid cell), and temperature exceedances beyond percentile thresholds are totaled
- The "shift ratio" is computed as exceedances of shifted distributions to exceedances expected from shifting a Gaussian distribution of equivalent length
- Statistically significant shift ratios are identified by shifting a Gaussian 0.5σ 10,000 times and tabulating the exceedances per shift. Grid cells where actual exceedances fall outside of the 5th to 95th percentile range of these 10,000 shifted Gaussian exceedances are deemed significantly non-Gaussian

For the cold side of the distribution, shift ratios greater than one represent longer-than-Gaussian tails, and shift ratios less than one represent shorter-than-Gaussian tails. For the warm side of the distribution, the opposite is true (see Figure S1 in supporting information). For example, a shift ratio of two for warm-side tails indicates there are twice as many extreme warm days exceeding the pre-shifted 95th-percentile threshold following a uniform 0.5σ warm shift than if the distribution were Gaussian. In this prototype for future warming, a sigma-based shift ensures that all distributions are shifted by the same amount relative to their

underlying variance. The value of 0.5σ provides a large enough shift to demonstrate the effect of non-Gaussian tail shape on threshold exceedances, but not so large as to overwhelm the effect of tail shape. Although related to distribution moments such as skewness and kurtosis, the shift ratio identifies non-Gaussianity specific to the tail rather than across the entire distribution. In addition to its physical interpretation, the shift ratio also acts as a variant on the Kolmogorov-Smirnov/Lilliefors test for normality as it applies to a random sampling procedure to test for significance of departures from Gaussianity in distribution tails (Loikith & Neelin, 2015).

Grid cells within spatially coherent regions of significant non-Gaussian tails are selected as cases to analyze horizontal characteristics of air parcel pathways associated with extreme surface temperatures and investigate the mechanisms governing tail shape within the region. Vertical characteristics did not contribute meaningfully to the analysis and are therefore not included. The grid cells chosen are also highlighted in related previous work (Loikith & Neelin, 2019; Loikith et al., 2018), and represent geographically diverse locations in the mid-latitudes where advection is often a dominant factor in extreme temperature development, especially in winter. This makes the application of a back-trajectory analysis particularly informative. Although the pathways by which extreme temperatures develop at individual locations may not represent those at other locations, analyses at the locations selected in this study are intended to provide a broad overview of the types of mechanisms that lead to shorter- and longer-than-Gaussian tails on both sides of the temperature distribution.

3.2. Back-Trajectory Analysis

To compute back-trajectories, the NOAA Air Resources Lab's Hybrid Single Particle Lagrangian Integrated Trajectory (HYSPLIT) model is employed (Stein et al., 2016). 48-h back-trajectories initialized at 12z 2 m above ground are generated for each extreme temperature day in the tail of the distribution at each location. Back trajectories are initialized using wind, pressure, relatively humidity, and temperature fields. Previous studies have applied HYSPLIT to explore the atmospheric flow patterns associated with pollutants (Hondula et al., 2010), precipitating storms (Bednorz, 2013), and extreme cold temperatures (Dimitriou et al., 2016). A trajectory length of 48 h is chosen as it is short enough to minimize pathway error (Stohl, 1998) while long enough to incorporate the influence of synoptic circulation on air parcel advection. Owing to the fine resolution of ERA5 and the three-dimensional variables for HYSPLIT, back-trajectories are computed using 3-hourly instantaneous data to reduce computational demand. Sampling the 5% warmest or coldest daily temperature anomalies for 1980–2014 generates 158 trajectories for DJF locations and 161 trajectories for JJA locations. However, if a back-trajectory extends into the month preceding the season (May for JJA or November for DJF), the entire trajectory is removed from analysis (<1.7% of trajectories). To analyze characteristics of synoptic-scale circulation associated with temperature extremes at select locations, composites of Z500 and anomalies are computed for days in the distribution tail and at 2 days prior. Significant relationships between tail days and recurrent modes of atmospheric and sea surface temperature variability are determined using the bootstrapping method with replacement.

4. Shift Ratio Results

Figure 1 displays shift ratios for both sides of the temperature distribution during DJF and JJA. Warm colors denote areas where a warm shift leads to more-rapid-than-Gaussian increases in warm (Figures 1a and 1b) or decreases in cold (Figures 1c and 1d) exceedances beyond a fixed threshold, whereas cool colors denote slower-than-Gaussian changes. Shift ratios reveal extensive, coherent regions of non-Gaussianity, such as shorter-than-Gaussian warm tails over Eurasia during DJF (Figure 1a), and longer-than-Gaussian cold tails over central South America during JJA (Figure 1d). In many cases, coherent regions of non-Gaussianity for cold-side tails are the opposite pattern to those exhibited by warm-side tails. For example, DJF warm-side shift ratios reveal shorter-than-Gaussian tails over Europe (Figure 1a) whereas cold-side shift ratios reveal longer-than-Gaussian tails (Figure 1c), which captures the negative skewness found in these regions. However, the spatial extent of significant shift ratios do not necessarily overlap. Furthermore, some locations experience short tails on both sides of the distribution, including southern Canada during DJF (Figures 1a and 1c), as well as two long tails, including India during JJA (Figures 1b and 1d). This highlights the utility of using the shift ratio to examine tails specifically. ERA5 shift ratio maps for both warm-side and cold-side

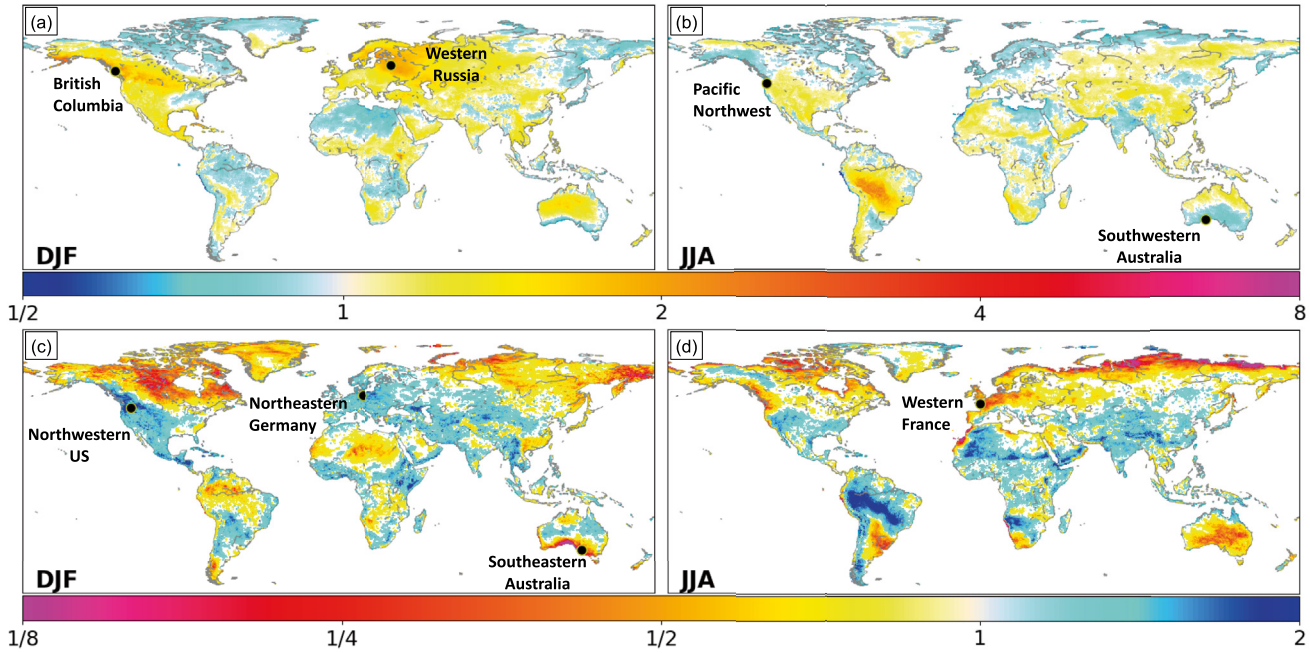

Figure 1. ERA5 Shift ratio maps for the (top) warm and (bottom) cold tails of the temperature distribution during (a and c) DJF and (b and d) JJA. Note the color bar reversal between warm-tail and cold-tail maps, as warm colors denote areas with significantly shorter-than-Gaussian tails (>1 on top, <1 on bottom), and cool colors denote areas with significantly longer-than-Gaussian tails (<1 on top, >1 on bottom). White areas over land are statistically indistinguishable from Gaussian at the 5% level. Locations selected for further analysis are identified. DJF, December, January, and February; JJA, June, July, and August.

tails closely resemble other observation-based and model datasets (Catalano et al., 2020; Loikith & Neelin, 2019; Loikith et al., 2018).

5. Non-Gaussian-Tailed Location Analysis

Eight grid cells within coherent regions of significant non-Gaussianity are selected (Figure 1): shorter-than-Gaussian warm-side (British Columbia, DJF, and Western Russia, DJF), longer-than-Gaussian warm-side (Pacific Northwest, JJA, and Southwestern Australia, JJA), shorter-than-Gaussian cold-side (Western France, JJA, and Southeastern Australia, DJF) and longer-than-Gaussian cold-side (Northwestern US, DJF, and Northeastern Germany, DJF). Refer to Figure S2 in the supporting information to visualize the tail departures from Gaussian. Diagnosis of tail behavior using a back-trajectory analysis is provided in subsequent sections, with one figure per location (Figures 4–11) organized as follows. The top row of each figure shows daily mean Z500 and anomaly composites on 2 days prior to and on extreme temperature days. The middle row shows back-trajectory density and individual back-trajectories. The bottom row shows two wind rose style panels ("trajectory roses") for 2 days and 1 day prior to extremes, with trajectories binned by cardinal and ordinal directions relative to the location along the azimuthal axis. For each gray-shaded wedge representing the percentage of trajectories, median distances from the location are along the radial axis, and median daily 2-m temperature differences relative to tail days are circles along the rose perimeter.

5.1. British Columbia—Winter Short Warm Tail

The British Columbia location (BCL) is on the Canadian Pacific coast with climatologically warmer air over the ocean to the south and west and cooler air inland during DJF (Figure 2a). BCL lies within a large, coherent region of significantly shorter-than-Gaussian warm tails across North America (Figure 1a). The synoptic environment up to 2 days prior to the warmest 5% of days is characterized by a large area of positive anomalies to the east and negative anomalies to the southwest, placing the location beneath an anomalous Z500 gradient (Figures a and b). The average Z500 pattern promotes mid-level southerly flow prior to warm extremes. Air parcels associated with the warmest DJF temperature days at BCL follow different pathways

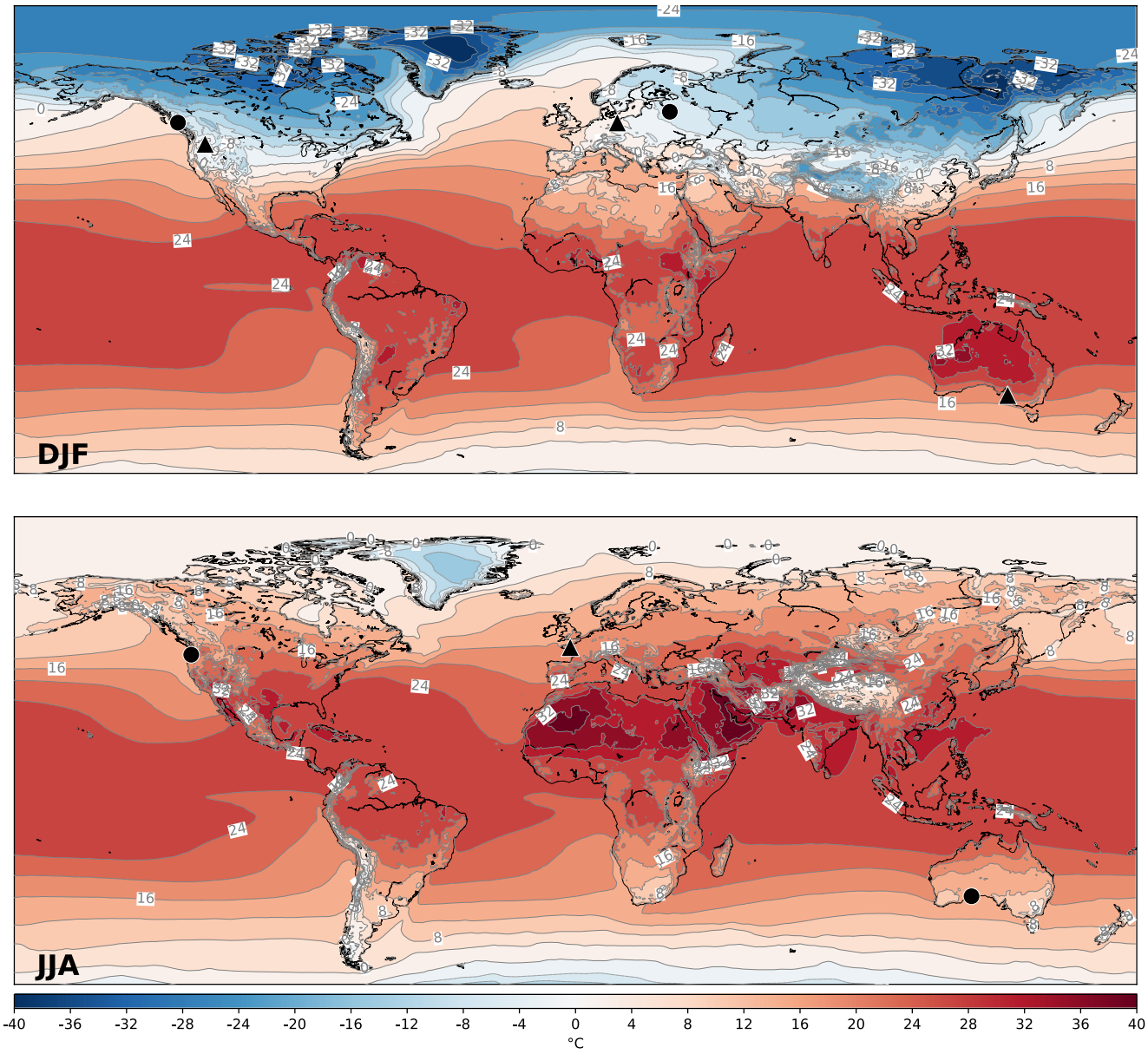

Figure 2. Two-meter temperature climatology for (a) DJF and (b) JJA, contoured every 4 °C. Black circles are selected locations analyzed for warm-tails, and black triangles are locations for cold-tails. DJF, December, January, and February; JJA, June, July, and August.

over land and ocean, however the highest frequency of back-trajectories originate to the south over the ocean and follow an inland route west of the Cascades into the Coast Mountains (Figures 3c and 3d).

Characteristics of back-trajectories at 2 days and 1 day prior to warm extremes are displayed in Figures 3e and 3f. Two days prior, 81.9% of back-trajectories are from southerly and southeasterly directions, with a smaller percentage from the southwest (Figure 3e). Median trajectory positions to the south and southwest are furthest from BCL (>960 km), indicating a faster rate of parcel motion compared with southeasterly trajectories (<460 km), likely owing in part to surface friction. Also, median daily 2-m temperature differences indicate that southerly and southwesterly parcels flow through a warmer environment 2 days prior than upon arrival at BCL, suggesting parcels cool sensibly over the ocean. One day prior, over three-quarters of trajectories are southeasterly over land at a median distance of 308.6 km from BCL, and average 2-m temperatures are only 0.3 °C warmer than upon arrival at BCL (Figure 3f). Thus, the majority of parcels

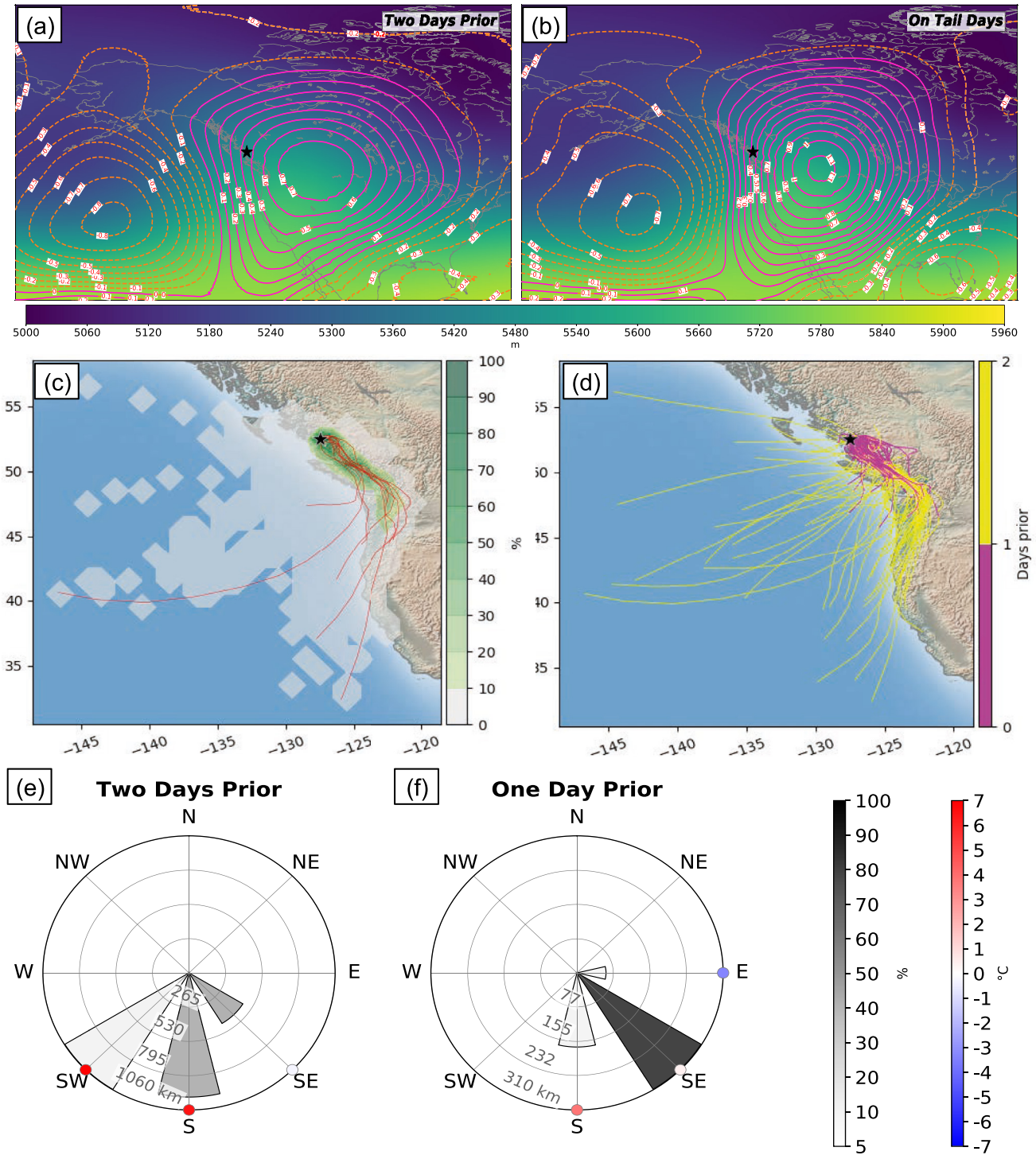

Figure 3. Circulation and air parcel transport associated with the warm tail of the DJF temperature distribution at British Columbia (black star). (Top row) Composite maps of daily 500-hPa geopotential height (shaded) and standardized anomalies (contoured) at (a) 2 days prior to extremes and (b) on warm-tail days. (Middle row) 48-h back-trajectories initialized at 12z on warm-tail days: (c) trajectory frequencies and trajectories associated with the 10 most extreme tail-day temperatures (red); (d) trajectory tracks, with colors representing 2 days (yellow) and 1 day (magenta) prior to extremes. (Bottom row) Trajectory roses representing the frequency (>5% shaded gray) of trajectories binned by angular direction (45° centered on cardinal and ordinal directions), as well as the median great circle distance relative to the location (radial coordinate in kilometer) and the median daily 2-m temperature difference relative to tail-day temperatures (filled circles in °C) at (e) 2 days and (f) 1 day prior to extremes. Note, instantaneous trajectory frequency, distance, and direction are at 12z, whereas temperature differences are computed from daily averages. DJF, December, January, and February.

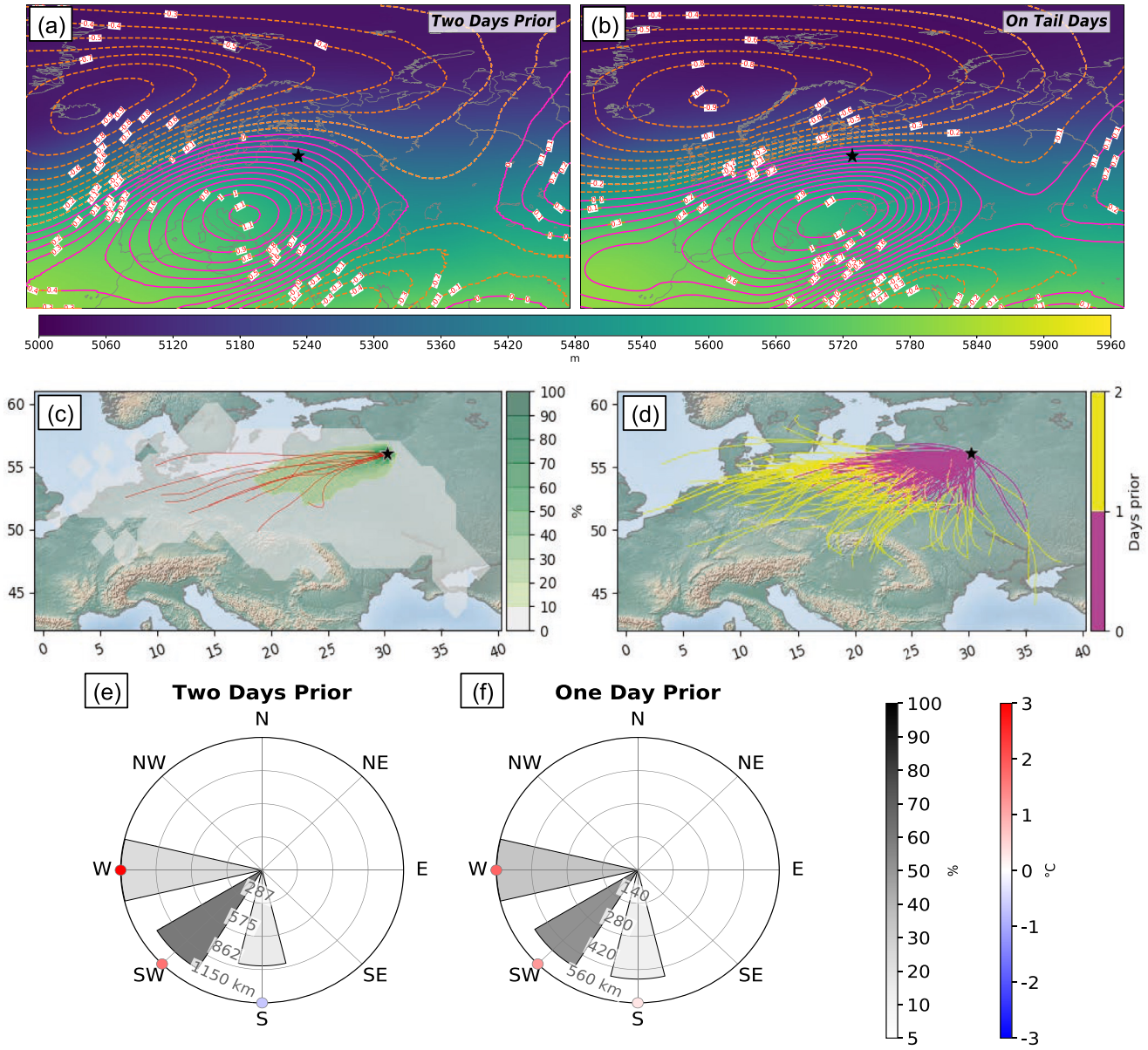

Figure 4. As in Figure 3, but for DJF warm-tail days at Western Russia. DJF, December, January, and February.

cool as they approach land, and temperatures are maintained while traveling inland and along the Strait of Georgia.

This analysis illustrates the process by which winter warm extremes develop at BCL, and thus why the warm tail is notably short along this coast. The warmest temperatures available for advection are to the south and southwest over the Pacific Ocean (Figure 2a), establishing an upper limit on temperatures at BCL. Underneath a synoptic setup promoting south/southwesterly flow (Figures 3a and 3b), the primary approach of air parcels is over the Pacific and terrain-following inland toward BCL from the southeast (Figures 3c and 3d), as less cooling occurs over land than ocean (Figures 3e and 3f). However, the moderation of temperatures by the ocean results in a short warm tail at BCL. Mechanisms for short warm tails likely differ further inland within this broad region of non-Gaussianity.

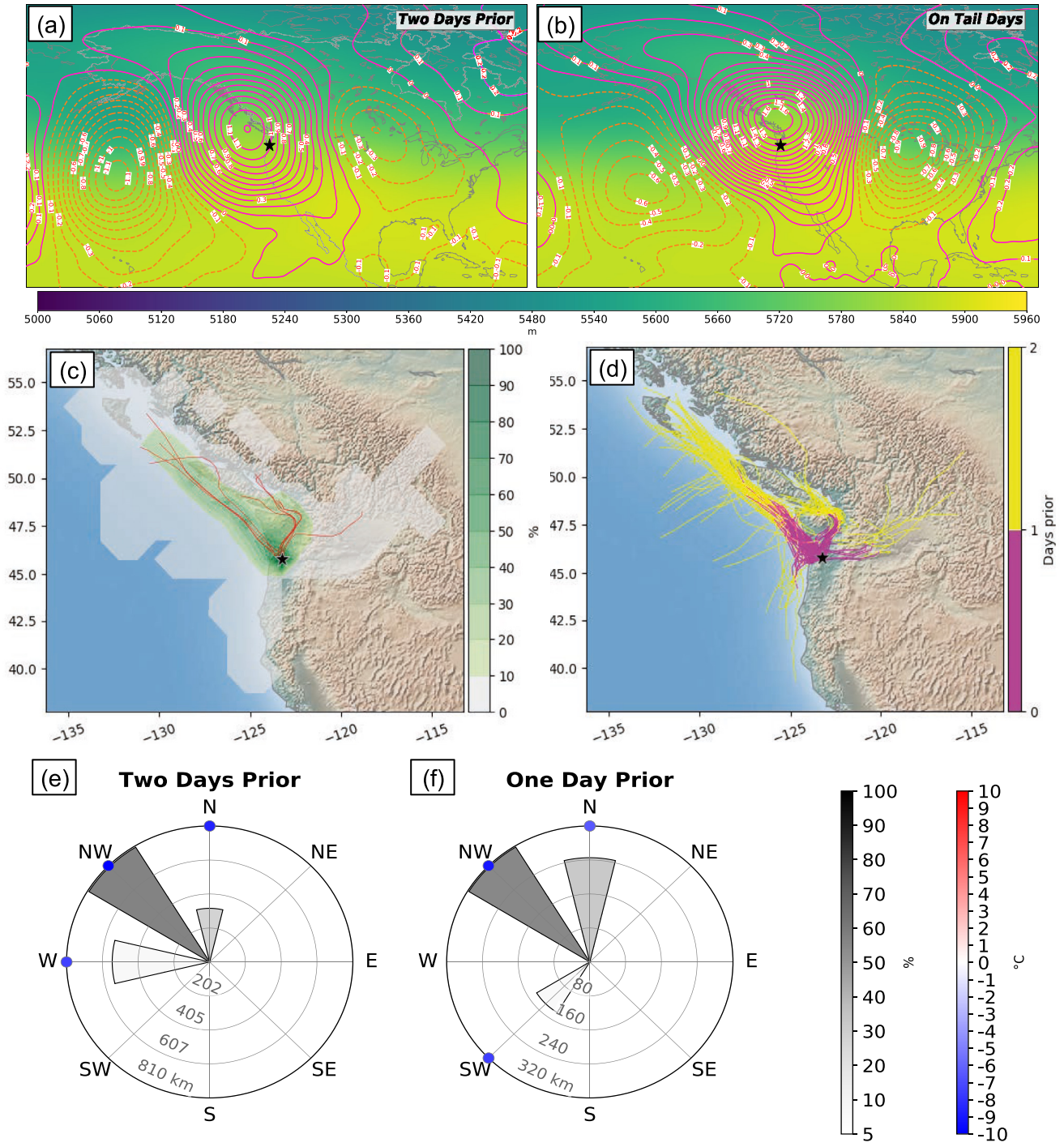

Figure 5. As in Figure 3, but for JJA warm-tail days at Pacific Northwest. JJA, June, July, and August.

5.2. Western Russia—Winter Short Warm Tail

The Western Russia location (WRL) is centered in a region of significantly shorter-than-Gaussian warm tails over Eurasia during DJF (Figure 1b). The regional climatological temperature gradient is relatively weak in winter, with warmer temperatures to the southwest and cooler temperatures northeast (Figure 2a). Anomalous 500-hPa ridging to the southwest and a deep trough northwest over the North Atlantic produce a steep anomaly gradient over WRL up to 2 days prior to warm extremes (Figures 4a and 4b). These

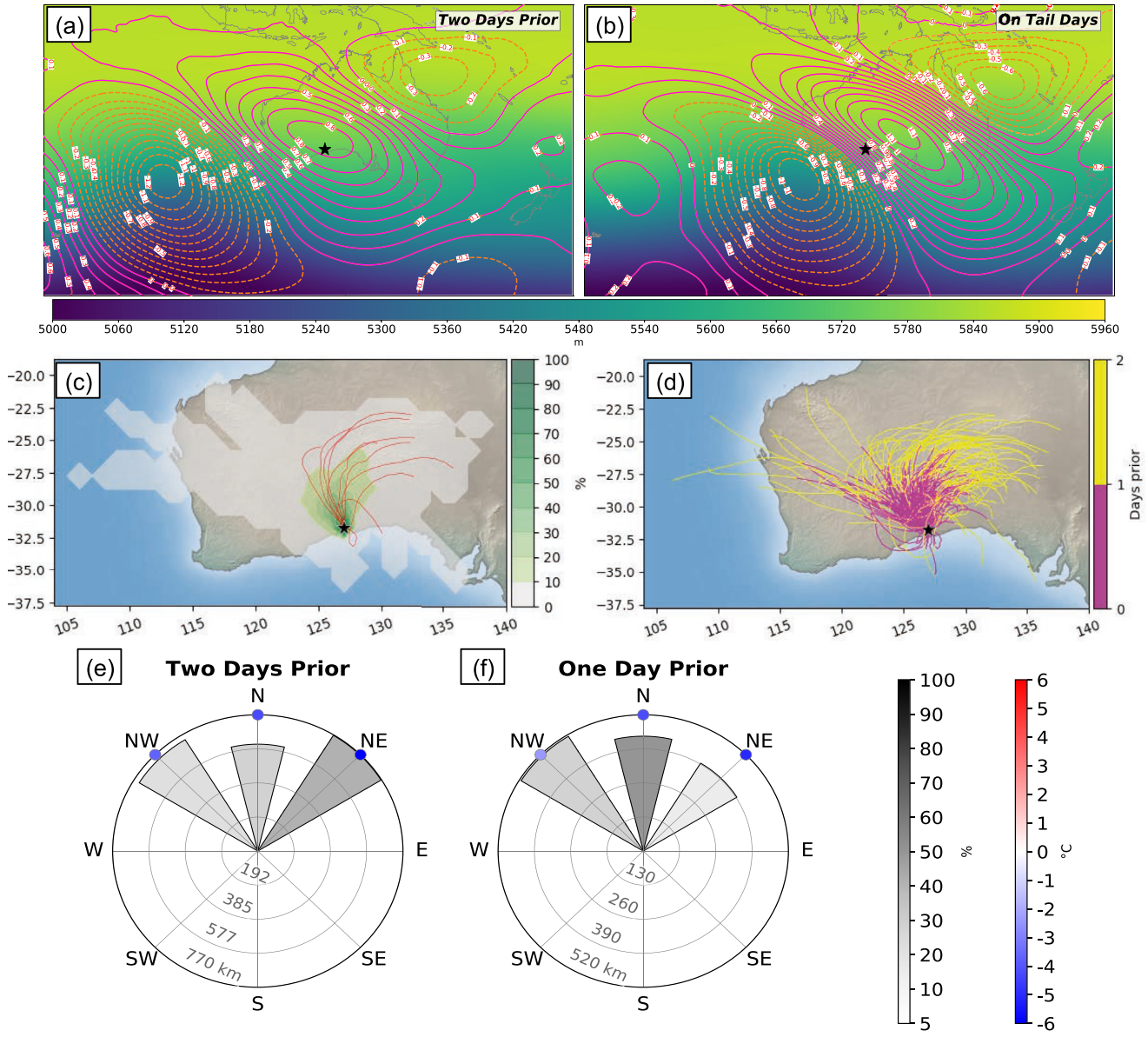

Figure 6. As in Figure 3, but for JJA warm-tail days at Southwestern Australia. JJA, June, July, and August.

anomalous heights yield Z500 values that promote mid-level southwesterly and westerly flow. Beneath this setup, individual trajectories follow a range of pathways from southerly to westerly across central Europe, with the highest frequency emerging to the west-southwest (Figures 4c and 4d).

Trajectory roses reveal that 83% of air parcels travel median distances >1,000 km toward WRL (Figure 4e). At 1 day prior, median distances are approximately half (Figure 4f), suggesting consistent advection transporting warmer air directly toward WRL. Surface temperatures are warmer along southwesterly and westerly trajectories at 2 days prior than on warm-tail days, though smaller differences by 1 day prior indicate cooling along the trajectory. A smaller percentage of back-trajectories to the south maintain marginal temperature differences. Back-trajectories are predominantly over land, so tail length is limited by the absence of source regions substantially warmer than the DJF climatological temperature at WRL. This differs from BCL where sea surface temperatures directly constrain warm extremes, cooling parcels sensibly over open ocean.

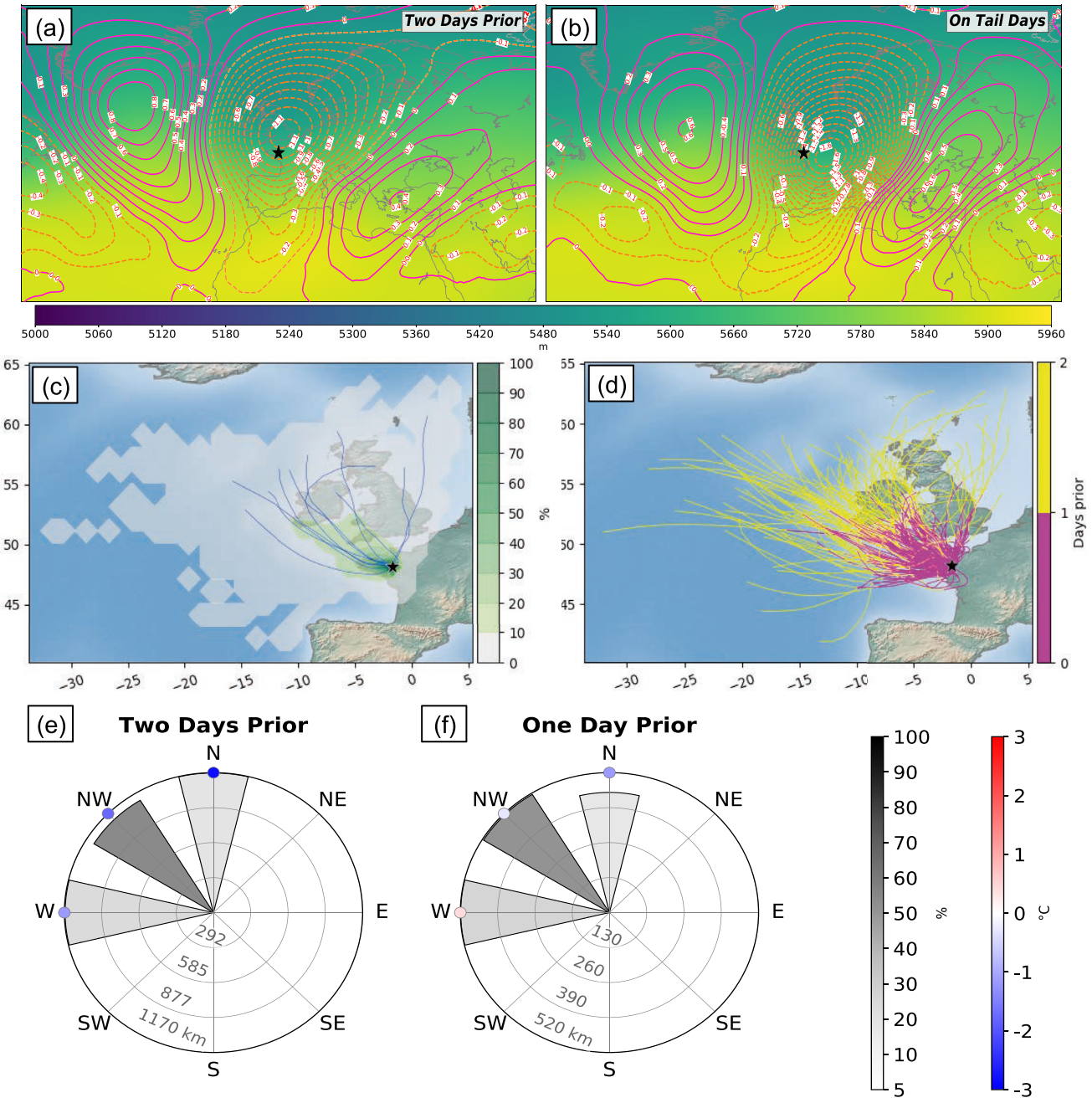

Figure 7. As in Figure 3, but for JJA cold-tail days at Western France. JJA, June, July, and August.

5.3. Pacific Northwest—Summer Long Warm Tail

The Pacific Northwest location (PNWL) is situated near the United States (US) Pacific Coast within a narrow region of longer-than-Gaussian warm-side tails along near-coastal zones during JJA (Figure 1b). Climatological temperatures are warmest to the south and east (Figure 2b). Two days prior to warm extremes, average synoptic circulation is comprised of anomalous 500-hPa ridging over the location and a maximum to the north-northwest (Figure 5a). By warm-tail days, the anomalous ridge intensifies and propagates to the north of PNWL (Figure 5b). Beneath this relatively persistent ridge, the majority of back-trajectories are northwesterly along the Pacific coast, with another cluster along the Juan de Fuca and Georgia Straits to the north (Figure 5c). Some air parcels also traverse the Snake River valley from the east, or along the California

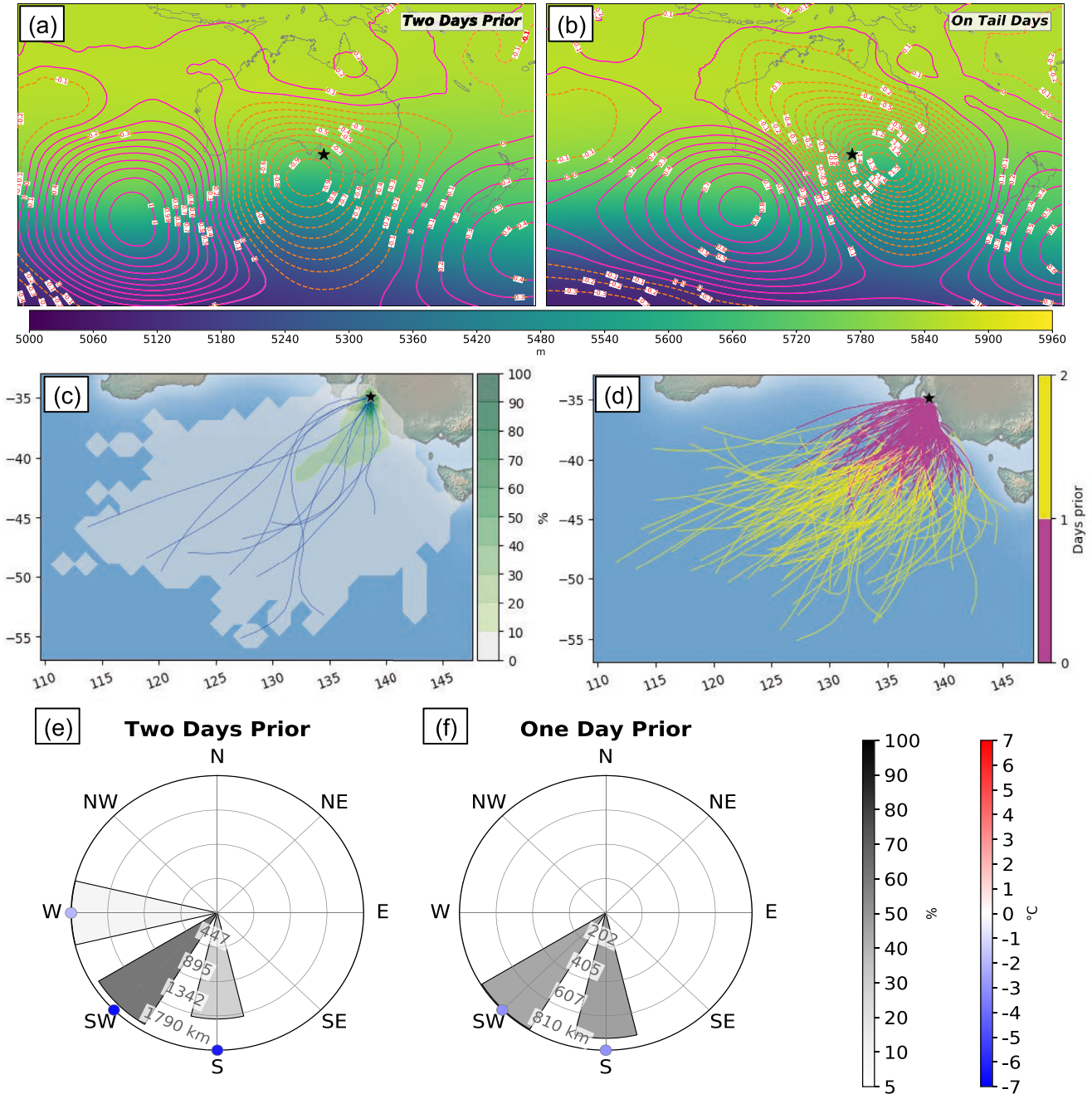

Figure 8. As in Figure 3, but for DJF cold-tail days at Southeastern Australia. DJF, December, January, and February.

coast (Figure 5d). Air parcels that bring the warmest temperatures originate from multiple sources to the northwest, north, and northeast 2 days prior to warm extremes at PNWL (Figure 5c), suggesting marine air does not sensibly cool parcels.

Over 80% of air parcels are positioned northwest or north of PNWL at both 1 day and 2 days prior to extremes, propagating through substantially cooler surface temperatures (<−6.5 °C) than on warm-tail days (Figures 5e and 5f). Thus, heat extremes manifest despite a trajectory pattern that would be expected to bring cooler air from the North. One likely mechanism for this phenomenon is the strong suppression of the marine layer under the Z500 ridge (Figures 5a and 5b), inhibiting the sensible cooling effects of the ocean (Elliott & O'Brien, 1977). This allows exceptionally warm temperatures, in an anomalous sense, to

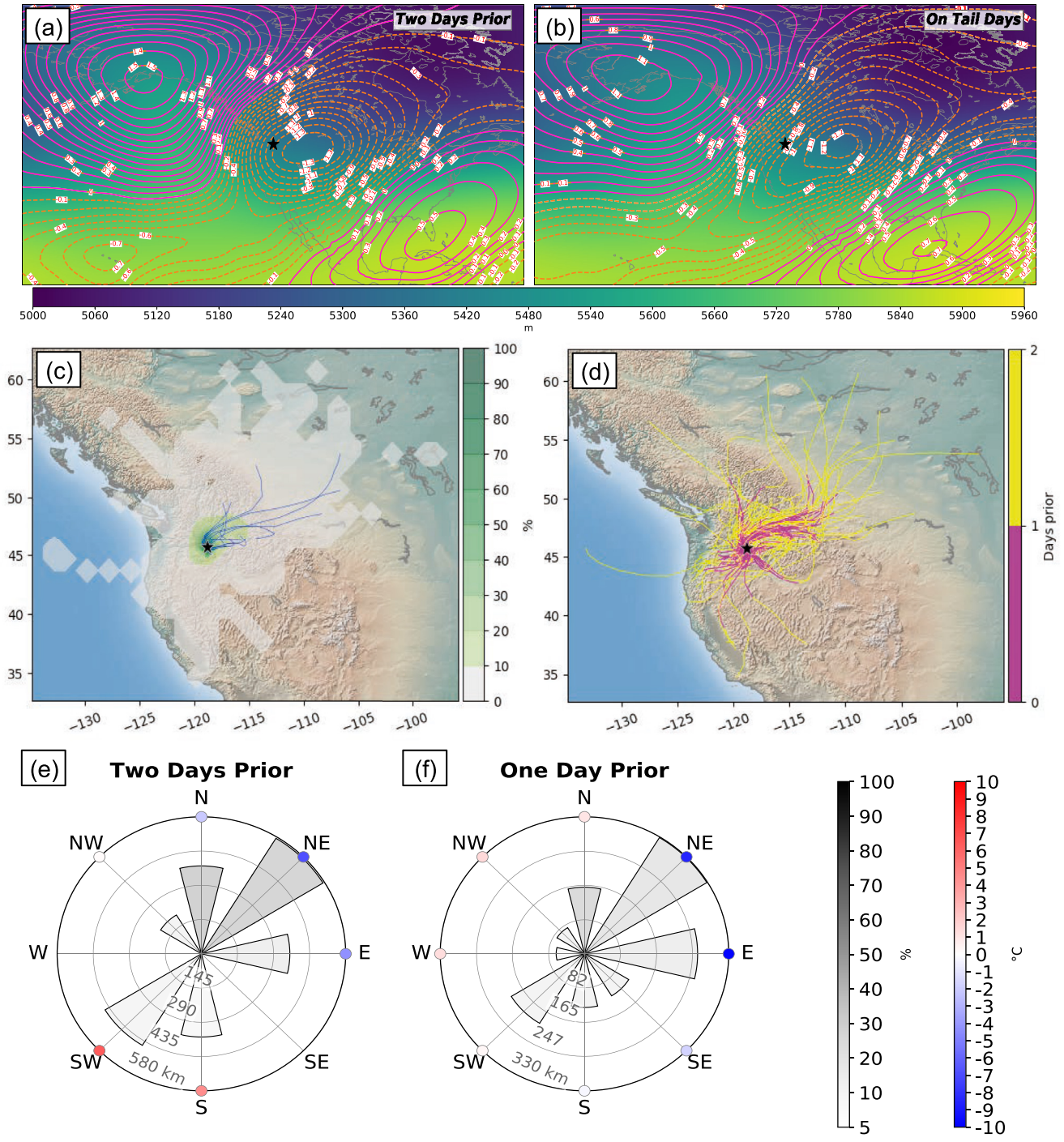

Figure 9. As in Figure 3, but for DJF cold-tail days at Northwestern US. DJF, December, January, and February.

develop. Vertical mixing may promote further warming owing to warm air advection above the lowest levels of the atmosphere. Also, the synoptic setup in Figures 5a and 5b is the principal circulation pattern for extreme heat waves (Bumbaco et al., 2013) and droughts (Gibson et al., 2020) in the region, and is conducive to the West Coast thermal trough, which often develops over California and extends northward (Brewer et al., 2012). Composite sea level pressure patterns reveal surface trough development (not shown), which is a result of diabatic heating. Therefore, unlike previous cases, the longer-than-Gaussian tail at PNWL is not a direct manifestation of anomalous advection, but rather processes that suppress the marine layer and

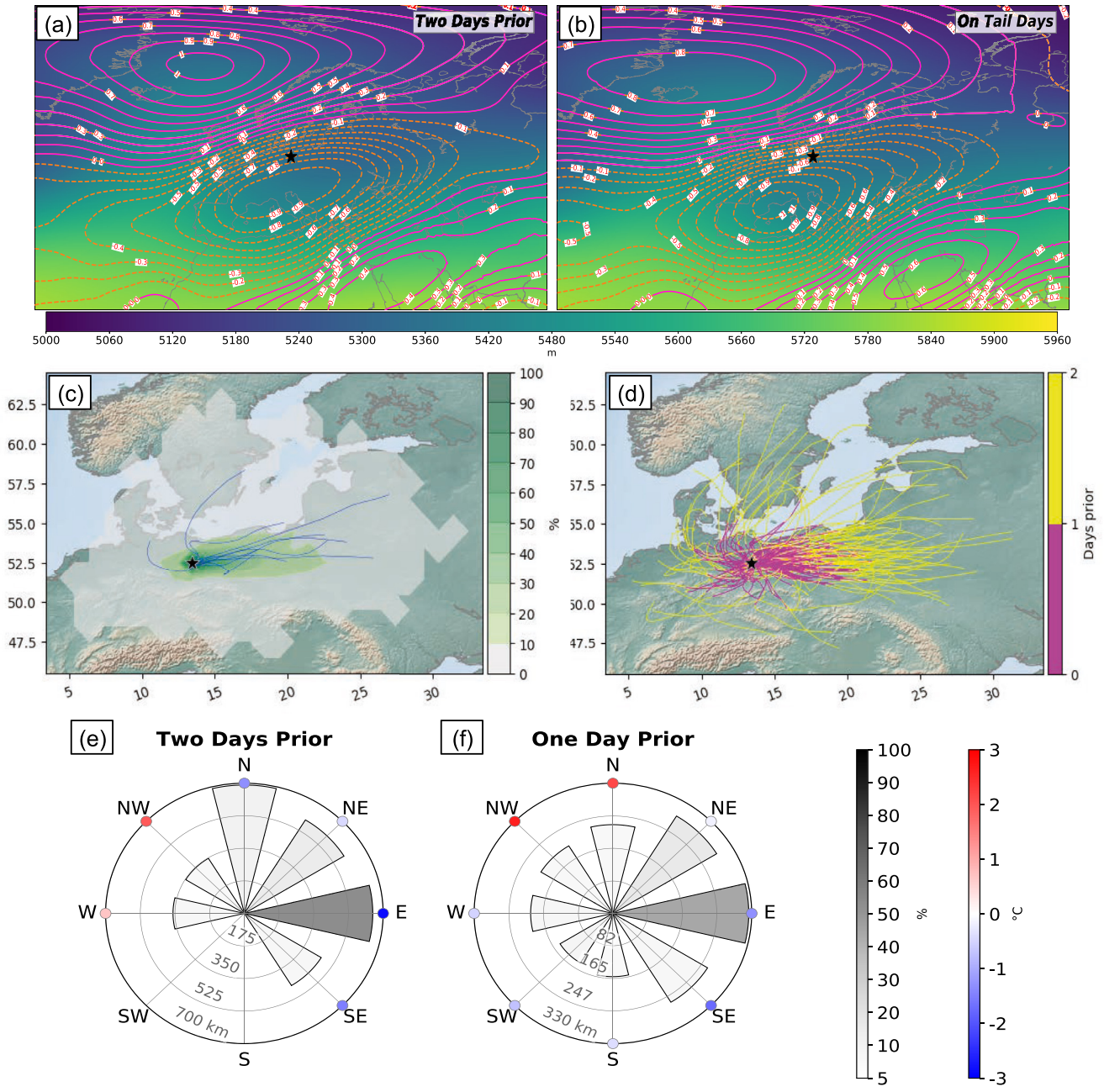

Figure 10. As in Figure 3, but for DJF cold-tail days at Northeastern Germany. DJF, December, January, and February.

inhibit low cloud development, thus allowing more shortwave absorption by the land surface so warm extremes depart notably from the mean.

5.4. Southwestern Australia—Winter Long Warm Tail

The Southwestern Australia location (SWAL) is in the Nullarbor Plain along the Southern Ocean within a coherent region of longer-than-Gaussian warm-side tails spanning the southern half of the continent (Figure 1b). Climatological temperatures over the adjacent ocean are similar to those over land, with warmer temperatures equatorward (Figure 2b). Z500 composites reveal an anomalous ridge tilted along a northwest-southeast axis above the location 2 days prior to warm extremes (Figure 6a), which progresses eastward

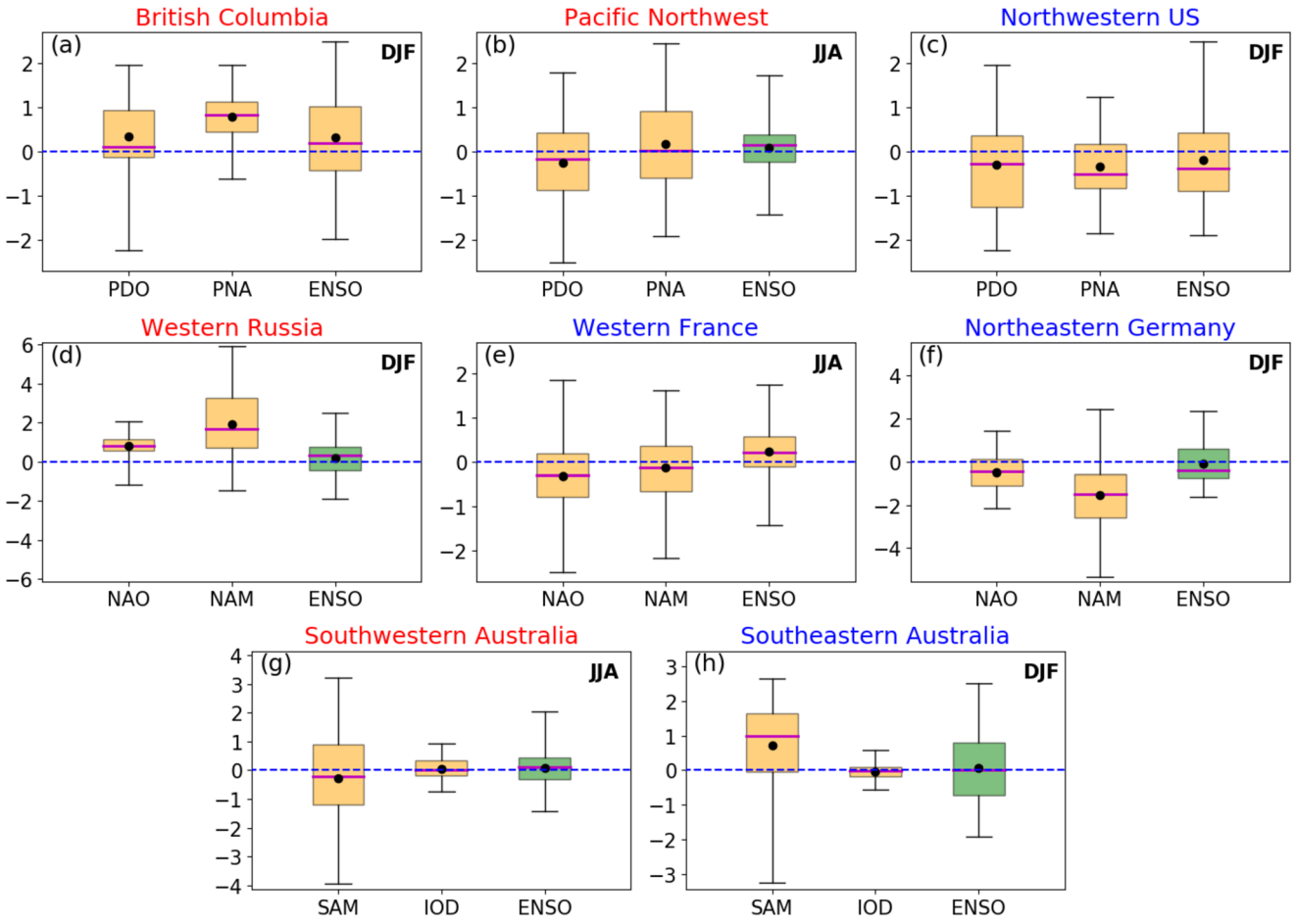

Figure 11. Box-and-whisker-plots displaying distributions of climate mode index values associated with extreme temperature days at select warm-tail (red) and cold-tail (blue) locations. Boxes identify the interquartile range from the 25th (bottom) to 75th (top) percentile, magenta lines represent the median, black dots represent the mean, and whiskers the full range of values. Green boxes indicate modes with mean values not significantly different from zero (blue dashed line) at the 5% level using bootstrapping. Note that presentation order is different from that used in above sections.

and results in a steep anomaly gradient over SWAL on warm-tail days (Figure 6b). Mid-level ridging and anticyclonic circulation at the surface centered east (not shown) yield northerly flow into the region. Most back-trajectories, including those associated with the warmest extremes, flow counterclockwise around the anticyclonic circulation and south into SWAL (Figures 6c and 6d).

Trajectory positions 2 days prior are northwesterly, northerly, and northeasterly <766.8 km from SWAL (Figure 7e). One day prior, half are northerly as air parcels descend into desert regions (Figure 6f), and median surface temperatures remain >2.3 °C cooler (Figures 6e and 6f). Although northerly advection of climatologically warmer air is associated with extreme temperature development at SWAL, the anomalous blocking pattern and offshore flow restricting cooler marine air is also important in producing large excursions from the mean. However, diabatic and adiabatic processes beneath strong ridging likely contribute to most extremes, and so cannot fully explain the notable longer-than-Gaussian warm tail here or across southern Australia (Figure 1b). One larger-scale governing condition for the broader long-tailed region that SWAL is within may be the poleward displacement of a relatively persistent high-pressure system at the surface (not shown) positively skewing the temperature distribution (Garfinkel & Harnik, 2017; Linz et al., 2018; Tamarin-Brodsky et al., 2019) as it draws in climatologically warmer air from the north. This differs from mechanisms of non-Gaussianity at other locations demonstrated in this study, which are related to more local features.

5.5. Western France—Summer Short Cold Tail

The Western France location (WFL) is characterized by a shorter-than-Gaussian cold tail during summer. Cold extremes develop beneath negative Z500 anomalies, with anomalous ridging to the northwest and southeast (Figure 7a). This wave train propagates downstream, with the trough deepening east of WFL and the encroaching ridge upstream tightening the gradient (Figure 7b). Z500 values promote mid-level westerly flow, and the corresponding sea level pressure gradient promotes low-level northwesterly flow (Loikith & Neelin, 2019) over the cooler North Atlantic (Figure 2b).

Two days prior, nearly all back-trajectories originate over the ocean, and the highest frequency of trajectories emerging to the west-northwest within 10° of WFL (Figures 7c and 7d). 54.1% of trajectory positions are located northwest of WFL and 24.2% are westerly 2 days prior, with comparable frequencies 1 day prior (Figures 7e and 7f). Median distances decline fairly uniformly, which suggests steady transport of parcels through a cooler, marine environment. However, median temperature differences are near-zero by 1 day prior, suggesting parcels warm sensibly en route. Similar to mechanisms at BCL, marine air limits how anomalously cold parcels can be upon arrival at WFL, explaining the significantly short cold tail.

5.6. Southeastern Australia—Summer Short Cold Tail

The Southeastern Australia location (SEAL) is situated in the foothills of the Flinders mountain range to the east and south of deserts spanning the continental interior. Thus, the most direct path to cold air during summer is over the Southern Ocean (Figure 2a). The synoptic environment consists of an anomalous 500-hPa trough over SEAL and an anomalous 500-hPa ridge to the southwest (Figures 8a and 8b) present for at least 4 days prior to extremes (Loikith & Neelin, 2019). The cloud of back-trajectory positions extends nearly 30° in longitude and 20° in latitude, indicating many pathways over the Southern Ocean for extreme cold air into SEAL (Figures 8c and 8d).

Two days prior to cold extremes, 98.7% of trajectory positions to the south and southwest are at a substantial median distance (>1,380 km) from SEAL (Figure 8e), though have traveled approximately half the distance by 1 day prior (Figure 8f). Along these pathways, median temperatures are >6 °C cooler 2 days prior but only about 3 °C cooler 1 day prior. The rapid speed at which air parcels travel (772 km on average over the final day, or 8.9 m s^{-1}) lessens the extent to which the ocean warms parcels, allowing temperatures to remain anomalously cold upon arrival. Analogous to WFL, steady advection through a marine environment moderates temperatures and yields a shorter-than-Gaussian cold tail at SEAL.

5.7. Northwestern US—Winter Long Cold Tail

The Northwestern US location (NWUSL) is in the Columbia Basin west of the Rocky Mountains, which separate the region from the downstream, coldest continental polar air. Thus, transport of exceptionally cold air from the interior only occurs in a highly anomalous synoptic environment. Composite circulation includes an anomalous trough centered east of NWUSL, tilted to the southeast, between two anomalous anticyclones over Alaska and the Gulf of Mexico (Figures 9a and 9b), a pattern which remains nearly stationary for at least 4 days prior to extremes (Loikith & Neelin, 2019). Back-trajectories reveal many pathways for cold extremes, with a cloud of points across the western US (Figure 9c). Although the main trajectory cluster is northeasterly, air parcels also travel from the Interior Plateau to the northwest and the Snake River Valley to the southeast, mostly following lower-elevation topography (Figure 9d). Some trajectories are southerly, though associated temperatures are in the warmer range of the cold tail (not shown). Pathway variability is likely a result of the complex topography of the region, with relatively dense, cold air preferentially traveling through lower elevations.

Two days prior to cold extremes, 54.8% of trajectory positions are north or northeast of NWUSL, whereas small percentages of trajectories are scattered among nearly all other directions (Figure 9e). Relative to other cases, the majority of trajectory positions are a short distance (<575 km) from NWUSL, which may be related to the surrounding terrain or weak low-level flow under high pressure. Along nearly all directions, median temperatures cool between 2 days and 1 day prior to extremes (Figures 9e and 9f), suggesting air parcels possibly cool radiationally under stable atmospheric conditions and minimal winter insolation or

as they traverse higher elevations (Loikith & Neelin, 2019). One day prior, northeasterly and easterly trajectories are furthest from NWUSL in an environment >8.5 °C cooler than associated tail-day temperatures, whereas trajectory positions from other directions travel <196.4 km through environments within 1.8 °C of tail-day extremes, on average.

There are multiple pathways for extreme cold temperature development at NWUSL. Complex topography interferes with air parcel transport, so many extreme cold temperatures result from air parcels sourced close to NWUSL within airmasses originating in the interior of North America. By 1 day prior, parcels have slowly propagated into the basin, where cold pools during winter can occur (Whiteman et al., 2001). However, pathways to the most extreme cold air outbreaks at NWUSL are associated with easterly and northeasterly trajectories from further distances (Figure 9c). This supports the hypothesis in Loikith et al. (2019) that the long cold tail in this region results from the coldest air being located downwind and across the physical barrier of the Rocky Mountains. As a result, extremely anomalously cold air can be transported into the region under rare and highly anomalous meteorological circumstances.

5.8. Northeastern Germany—Winter Long Cold Tail

The Northeastern Germany location (NEGL) is in the North European Plain near sea level, within a region of significantly longer-than-Gaussian cold tails across Europe (Figure 1c). Climatologically colder temperatures are located to the north and east during winter (Figure 2a), though prevailing winds in this region are westerly. Thus, a rare reversal in flow is essential to the development of cold extremes at NEGL through transport from the continental interior of Eurasia. Up to 4 days prior to cold-tail days (Loikith & Neelin, 2019), mid-level circulation is comprised of an anomalous trough centered south of NEGL (Figures 10a and 10b). Composite sea level pressure resembles a blocking pattern with a gradient strengthening over NEGL (Loikith & Neelin, 2019), promoting easterly flow into the region.

Although some air parcels travel from southern and northern Europe, a core cluster of back-trajectories follows direct pathways from the east, including those associated with the coldest extremes at NEGL (Figures 10c and 10d). 53.2% of trajectory positions are located at a median distance of 647.6 km eastward, with smaller percentages of trajectories traveling from other directions 2 days prior to extremes (Figure 10e). One day prior, positions are scattered in all directions relative to NEGL, though 44.9% of trajectories remain easterly (Figure 10f) owing to steady advection beneath a favorable, anomalous synoptic setup (Figures 10a and 10b). Easterly parcels propagate at higher speeds relative to other directions, which reduces sensible warming (Figures 10e and 10f). The long tail is the result of similar conditions as NWUSL except without the topographic barrier.

5.9. Teleconnection Patterns

Figure 11 displays box-and-whisker plots indicating distribution percentiles of index values concurrent with extreme temperature days at select locations for modes of climate variability that have been shown to influence extreme temperatures in these regions (Hendon et al., 2007; Loikith & Broccoli, 2014; Ning & Bradley, 2015; Saji et al., 2005; Thompson & Wallace, 2001). Although oscillation timescales range from interannual to multidecadal, this analysis provides broad context for the likelihood of extremes in associated anomalous environments, highlighting where climate modes provide favorable background conditions for the occurrence of extremes.

At all locations, indices associated with extremes range from negative to positive, though extreme temperature days are more likely to occur during certain phases in some cases. The majority of warm-tail days at BCL are associated with positive Pacific Decadal Oscillation (PDO), which generally denotes warmer sea surface temperatures along the adjacent Pacific Coast, as well as positive ENSO (Figure 11a), which can amplify the response when in phase with PDO (Fleming & Whitfield, 2010). Also, 92.9% of extreme warm temperature days are associated with positive Pacific North-American Pattern (PNA) indices (Figure 11a), leading to above-average heights over BCL at 500-hPa (Figures 3a and 3b). These patterns support warm advection of marine air into BCL, which contributes to the shorter-than-Gaussian winter warm tail. Relationships with climate modes at PNWL are less robust than at BCL. JJA warm-tail days are mostly associated with negative PDO indices (Figure 11b), suggesting ocean temperatures do not influence summer warm

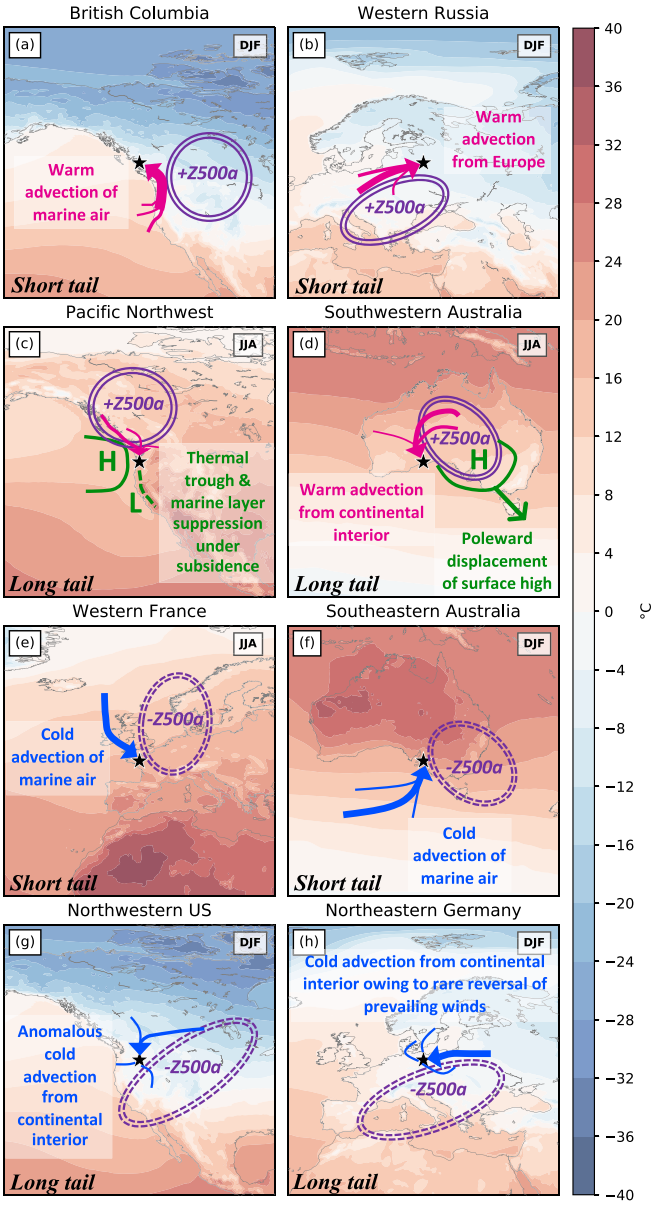

Figure 12. Summary of primary mechanisms governing non-Gaussian temperature distribution tail behavior at select locations (black stars). Magenta and blue arrows represent principal pathways for warm and cold extremes, respectively, with thickness related to back-trajectory frequency. Pressure systems are in green, and 500-hPa geopotential height anomalies are in purple. Climatological temperatures are shaded.

extremes at PNWL. Also, 50.6% of warm-tail days are associated with positive PNA indices, and the mean ENSO index is insignificantly different from zero. On cold-tail days at NWUSL, all three patterns are significantly negative (Figure 11c). Negative PDO and negative ENSO indicate cooler temperatures in western North America (Mantua et al., 1997; Smith & Sardeshmukh, 2000), and negative PNA involves a ridge over Alaska (Figures 9a and 9b), all of which contribute to cold extremes in the region.

At WRL, 93.6% and 86.5% of warm-tail days occur during positive North Atlantic Oscillation (NAO) and Northern Annular Mode (NAM) indices, respectively (Figure 11d). These patterns involve above-average heights over northern Europe (Figures 4a and 4b), and have been shown to strengthen prevailing westerly flow across Europe during winter (Osborn, 2006). This confines cold air to the interior while transporting milder air toward WRL. For cold-side tails, the opposite pattern is present over Europe. Median NAO and NAM indices are significantly negative at both WFL and NEGL (Figures 11e and 11f), and are generally associated with anomalous Z500 troughs over western Europe (Figures 8a, 8b, 11a, and 11b). ENSO is insignificantly different from zero at WRL and NEGL, whereas most cold extreme days at WFL are associated with positive ENSO indices. However, this statistical relationship remains physically unclear, as previous research indicates a weaker, lagged response over Europe during summer (Kiladis & Diaz, 1989; Moron & Ward, 1998).

SWAL winter warm-tail days are associated with negative Southern Annual Mode (SAM) and positive Indian Ocean Dipole (IOD) indices (Figure 11g), whereas SEAL summer cold-tail days occur during opposite patterns. SAM is positive on nearly three-quarters of cold-tail days at SEAL during DJF (Figure 11h) and is associated with a strengthening of prevailing westerlies and higher pressure over southern Australia. At both locations, relationships with IOD are less pronounced, which supports prior work suggesting lower correlations during these seasons (Saji et al., 2005). Also, the mean ENSO index is insignificantly different from zero, as Jones and Trewin (2000) showed temperatures are weakly correlated with ENSO.

6. Summary and Discussion

Using a back-trajectory analysis, we illuminate the mechanisms leading to non-Gaussian tails at eight geographically diverse extratropical locations (summarized in Figure 12). This work focuses on extratropical locations, since at lower latitudes, intrinsically narrower temperature distributions make tail length less important for future changes in exceedance frequency (Fischer et al., 2012). This occurs because in a narrow distribution, even a modest warming moves a substantial portion of the entire distribution to values above a fixed temperature threshold. This results in large changes in exceedances frequency that are not primarily dependent on characteristics of the tail.

Short-tailed locations British Columbia, Western France, and Southeastern Australia are proximate to the ocean, so advection from these marine sources acts to limit how extreme temperatures can be. The shorter-than-Gaussian tail at Western Russia is a result of advection over a climatologically weak temperature gradient (Figures 12a, 12b, 12e, and 12f). Long cold-tailed locations require rare, highly anomalous meteorological conditions in winter to transport cold air from climatologically downstream locations and/or across physical barriers (Figures 12g and 12h). Advection-based processes are less important at the long

warm-tailed Pacific Northwest where occasional suppression of the marine layer is key (Figure 12c). The long warm tail at Southwestern Australia, on the other hand, likely results from broader scale meridional movement of eddy stirring (Figure 12d; Garfinkel & Harnik, 2017; Linz et al., 2018). Furthermore, while not presented here, assessment of potential temperatures along trajectory pathways indicates some influence of diabatic processes modulating parcel temperatures along the transport pathway. Cases analyzed here represent only some of the global coherent regions of non-Gaussianity, however findings are likely extensible to many locations. Some cases exhibit a relationship between the occurrence of extremes and preferred sign and magnitude of influential recurrent modes of climate variability, providing background conditions conducive to, but not necessary for, the local meteorological setups that lead to days in the tail.

Results contribute to recent and ongoing research into the atmospheric drivers of temperature distribution skewness and implications for global warming. For example, Tamarin-Brodsky et al. (2019) employ a Lagrangian feature-tracking technique to understand how full distribution skewness is manifested through meridional temperature advection. While our results largely support advection as a key driver of extremes and tail length, by taking a local perspective using a parcel-trajectory approach, we further demonstrate that the atmospheric mechanisms governing tail non-Gaussianity vary based on physical geography and regional climatology.

Cold-tailed locations approximate those in Loikith and Neelin (2019), expanding on the understanding of extreme temperatures at non-Gaussian-tailed locations. However, the focus on mid-latitude, primarily synoptically driven examples may not capture all mechanisms for tail non-Gaussianity. For example, land-atmosphere interactions have also been shown to influence extreme temperatures (Mueller & Seneviratne, 2012) and higher-order distribution moments (Berg et al., 2014). Furthermore, many regions of non-Gaussianity have not been analyzed, including long cold tails in central South America during JJA, though Prince and Edwards (2018) document Andean cold surge events as likely primary drivers of cold extremes in this region. The shift ratio utilized in this work provides a pragmatic demonstration of how tail shape affects extreme temperatures under the simplest prototype for a warming climate, a uniform warm shift of the distribution. This metric has been shown to be a reasonable approximation of future changes in warm extremes (Loikith et al., 2018). However, McKinnon et al. (2016) demonstrated that trends in summer extremes over the historical period include significant changes in kurtosis and skewness, which could have an appreciable effect on the frequency of extremes as temperatures rise (Ballester et al., 2010; Clark et al., 2006). The latest ensemble of global climate models, CMIP6, skillfully captures coherent regions of non-Gaussian tails (Catalano et al., 2020), so additional work analyzing the complexity of projected changes in the distribution of temperature extremes would be beneficial.

Data Availability Statement

Climate mode indices are publicly available through https://www.cpc.ncep.noaa.gov/products/precip/CWlink/daily_ao_index/teleconnections.shtml, http://research.jisao.washington.edu/pdo/PDO.latest.txt, https://psl.noaa.gov/gcos_wgsp/Timeseries/Data/dmi.had.long.data, and https://climexp.knmi.nl/data/ihadisst1_nino3.4a.dat, and ERA5 through https://climate.copernicus.eu/climate-reanalysis

Acknowledgments
Support for this work is provided by the U.S. National Science Foundation through Grant AGS-1621554.

References

Ballester, J., Giorgi, F., & Rodó, X. (2010). Changes in European temperature extremes can be predicted from changes in PDF central statistics. *Climatic Change*, *98*, 277–284. https://doi.org/10.1007/s10584-009-9758-0

Bednorz, E. (2013). Synoptic conditions of heavy snowfalls in Europe. *Geografiska Annaler: Series A, Physical Geography*, *95*, 67–78. https://doi.org/10.1111/geoa.12001

Berg, A., Lintner, B. R., Findell, K. L., Malyshev, S., Loikith, P. C., & Gentine, P. (2014). Impact of soil moisture-atmosphere interactions on surface temperature distribution. *Journal of Climate*, *27*, 7976–7993. https://doi.org/10.1175/jcli-d-13-00591.1

Brewer, M. C., Mass, C. F., & Potter, B. E. (2012). The west coast thermal trough: Climatology and synoptic evolution. *Monthly Weather Review*, *140*, 3820–3843. https://doi.org/10.1175/mwr-d-12-00078.1

Bumbaco, K. A., Dello, K. D., & Bond, N. A. (2013). History of Pacific Northwest heat waves: Synoptic pattern and trends. *Journal of Applied Meteorology and Climatology*, *52*, 1618–1631. https://doi.org/10.1175/jamc-d-12-094.1

Catalano, A. J., Loikith, P. C., & Neelin, J. D. (2020). Evaluating CMIP6 model fidelity at simulating non-Gaussian temperature distribution tails. *Environmental Research Letters*, *15*, 074026. https://doi.org/10.1088/1748-9326/ab8cd0

Cavanaugh, N. R., & Shen, S. S. P. (2014). Northern hemisphere climatology and trends of statistical moments documented from GHCN-daily surface air temperature station data from 1950 to 2010. *Journal of Climate*, *27*, 5396–5410. https://doi.org/10.1175/jcli-d-13-00470.1

Clark, R. T., Brown, S. J., & Murphy, J. M. (2006). Modeling Northern Hemisphere summer heat extreme changes and their uncertainties using a physics ensemble of climate sensitivity experiments. *Journal of Climate*, *19*, 4418–4435. https://doi.org/10.1175/jcli3877.1

Dimitriou, K., McGregor, G. R., Kassomenos, P. A., & Paschalidou, A. K. (2016). Exploring winter mortality variability in five regions of England using back trajectory analysis. *Earth Interactions*, *20*, 27p. https://doi.org/10.1175/ei-d-15-0012.1

Easterling, D. R. (2002). Recent changes in frost days and the frost-free season in the United States. *Bulletin of the American Meteorological Society*, *83*, 1327–1332. https://doi.org/10.1175/1520-0477-83.9.1327

Elliott, D. L., & O'Brien, J. J. (1977). Observational studies of the marine boundary layer over an upwelling region. *Monthly Weather Review*, *105*, 86–98. https://doi.org/10.1175/1520-0493(1977)105<0086:osotmb>2.0.co;2

Fischer, E. M., Oleson, K. W., & Lawrence, D. M. (2012). Contrasting urban and rural heat stress responses to climate change. *Geophysical Research Letters*, *39*, L03705. https://doi.org/10.1029/2011gl050576

Fleming, S. W., & Whitfield, P. H. (2010). Spatiotemporal mapping of ENSO and PDO surface meteorological signals in British Columbia, Yukon, and southeast Alaska. *Atmosphere-Ocean*, *48*(2), 122–131. https://doi.org/10.3137/ao1107.2010

Garfinkel, C. I., & Harnik, N. (2017). The non-Gaussianity and spatial asymmetry of temperature extremes relative to the storm track: The role of horizontal advection. *Journal of Climate*, *30*, 445–464. https://doi.org/10.1175/jcli-d-15-0806.1

Gibson, P. B., Waliser, D. E., Guan, B., DeFlorio, M. J., Ralph, F. M., & Swain, D. L. (2020). Ridging associated with drought across the western and southwestern United States: Characteristics, trends, and predictability sources. *Journal of Climate*, *33*, 2485–2508. https://doi.org/10.1175/jcli-d-19-0439.1

Gross, M. H., Donat, M. G., & Alexander, L. V. (2019). Changes in daily temperature extremes relative to the mean in coupled model intercomparison project phase 5 models and observations. *International Journal of Climatology*, *39*(14), 5273–5291. https://doi.org/10.1002/joc.6138

Grotjahn, R., Black, R., Leung, R., Wehner, M. F., Barlow, M., Bosilovich, M., et al. (2016). North American extreme temperature events and related large scale meteorological patterns: A review of statistical methods, dynamics, modeling, and trends. *Climate Dynamics*, *46*, 1151–1184. https://doi.org/10.1007/s00382-015-2638-6

Hendon, H. H., Thompson, D. W. J., & Wheeler, M. C. (2007). Australian rainfall and surface temperature variations associated with the southern hemisphere annular mode. *Journal of Climate*, *20*, 2452–2467. https://doi.org/10.1175/jcli4134.1

Hersbach, H., Bell, B., Berrisford, P., Hirahara, S., Horányi, A., Muñoz-Sabater, J., et al. (2020). The ERA5 global reanalysis. *The Quarterly Journal of the Royal Meteorological Society*. https://doi.org/10.1002/qj.3803

Hondula, D. M., Sitka, L., Davis, R. E., Knight, D. B., Gawtry, S. D., Deaton, M. L., et al. (2010). A back-trajectory and air mass climatology for the Northern Shenandoah Valley, USA. *International Journal of Climatology*, *30*(4), 569–581. https://doi.org/10.1002/joc.1896

Horel, J. D., & Wallace, J. M. (1981). Planetary-scale atmospheric phenomena associated with the Southern Oscillation. *Monthly Weather Review*, *109*, 813–829. https://doi.org/10.1175/1520-0493(1981)109<0813:psapaw>2.0.co;2

Hurrell, J. W. (1995). Decadal trends in the North Atlantic Oscillation: Regional temperatures and precipitation. *Science*, *269*, 676–679. https://doi.org/10.1126/science.269.5224.676

Jones, D. A., & Trewin, B. C. (2000). On the relationships between the El Niño-Southern Oscillation and Australian land surface temperature. *International Journal of Climatology*, *20*, 697–719. https://doi.org/10.1002/1097-0088(20000615)20:7<697::aid-joc499>3.0.co;2-a

Kharin, V. V., Zwiers, F. W., Zhang, X., & Wehner, M. (2013). Changes in temperature and precipitation extremes in the CMIP5 ensemble. *Climatic Change*, *119*, 345–357. https://doi.org/10.1007/s10584-013-0705-8

Kiladis, G. N., & Diaz, H. F. (1989). Global climatic anomalies associated with extremes in the southern oscillation. *Journal of Climate*, *2*, 1069–1090. https://doi.org/10.1175/1520-0442(1989)002<1069:gcaawe>2.0.co;2

Lehner, B., Döll, P., Alcamo, J., Henrichs, T., & Kaspar, F. (2006). Estimating the impact of global change on flood and drought risks in Europe: A continental, integrated analysis. *Climatic Change*, *75*, 273–299. https://doi.org/10.1007/s10584-006-6338-4

Limpasuvan, V., & Hartmann, D. L. (1999). Eddies and the annular modes of climate variability. *Geophysical Research Letters*, *26*, 3133–3136. https://doi.org/10.1029/1999gl010478

Linz, M., Chen, G., & Hu, Z. (2018). Large-scale atmospheric control on non-Gaussian tails of midlatitude temperature distributions. *Geophysical Research Letters*, *45*, 9141–9149. https://doi.org/10.1029/2018gl079324

Loikith, P. C., & Broccoli, A. J. (2012). Characteristics of observed atmospheric circulation patterns associated with temperature extremes over North America. *Journal of Climate*, *25*, 7266–7281. https://doi.org/10.1175/jcli-d-11-00709.1

Loikith, P. C., & Broccoli, A. J. (2014). The influence of recurrent modes of climate variability on the occurrence of winter and summer extreme temperatures over North America. *Journal of Climate*, *27*(4), 1600–1618. https://doi.org/10.1175/jcli-d-13-00068.1

Loikith, P. C., & Neelin, J. D. (2015). Short-tailed temperature distributions over North America and implications for future changes in extremes. *Geophysical Research Letters*, *42*, 8577–8585. https://doi.org/10.1002/2015gl065602

Loikith, P. C., & Neelin, J. D. (2019). Non-Gaussian cold-side temperature distribution tails and associated synoptic meteorology. *Journal of Climate*, *32*, 8399–8414. https://doi.org/10.1175/jcli-d-19-0344.1

Loikith, P. C., Neelin, J. D., Meyerson, J., & Hunter, J. S. (2018). Short warm-side temperature distribution tails drive hot spots of warm temperature extreme increases under near-future warming. *Journal of Climate*, *31*, 9469–9487. https://doi.org/10.1175/jcli-d-17-0878.1

Mantua, N. J., Hare, S. R., Zhang, Y., Wallace, J. M., & Francis, R. C. (1997). A Pacific interdecadal climate oscillation with impacts on salmon production. *Bulletin of the American Meteorological Society*, *78*, 1069–1079. https://doi.org/10.1175/1520-0477(1997)078<1069:apicow>2.0.co;2

McKinnon, K. A., Rhines, A., Tingley, M. P., & Huybers, P. (2016). The changing shape of Northern Hemisphere summer temperature distributions. *Journal of Geophysical Research: Atmospheres*, *121*, 8849–8868. https://doi.org/10.1002/2016jd025292

Moron, V., & Ward, M. N. (1998). ENSO teleconnections with climate variability in the European and African sectors. *Weather*, *53*, 287–295. https://doi.org/10.1002/j.1477-8696.1998.tb06403.x

Mueller, B., & Seneviratne, S. I. (2012). Hot days induced by precipitation deficits at the global scale. *Proceedings of the National Academy of Sciences of the United States of America*, *109*, 12398–12403. https://doi.org/10.1073/pnas.1204330109

Ning, L., & Bradley, R. S. (2015). Winter climate extremes over the northeastern United States and southeastern Canada and teleconnections with large-scale modes of climate variability. *Journal of Climate*, *28*, 2475–2493. https://doi.org/10.1175/jcli-d-13-00750.1

Osborn, T. J. (2006). Recent variations in the winter North Atlantic Oscillation. *Weather*, *61*, 353–355. https://doi.org/10.1256/wea.190.06

Perron, M., & Sura, P. (2013). Climatology of non-Gaussian atmospheric statistics. *Journal of Climate*, *26*, 1063–1083. https://doi.org/10.1175/jcli-d-11-00504.1

Pfahl, S. (2014). Characterising the relationship between weather extremes in Europe and synoptic circulation features. *Natural Hazards and Earth System Sciences*, *14*(6), 1461–1475. https://doi.org/10.5194/nhess-14-1461-2014

Prince, K. C., & Evans, C. (2018). A climatology of extreme South American Andean cold surges. *Journal of Applied Meteorology and Climatology*, *57*, 2297–2315. https://doi.org/10.1175/jamc-d-18-0146.1

Saji, N. H., Ambrizzi, T., & Ferraz, S. E. T. (2005). Indian Ocean Dipole mode events and austral surface air temperature anomalies. *Dynamics of Atmospheres and Oceans*, *39*, 87–101. https://doi.org/10.1016/j.dynatmoce.2004.10.015

Saji, N. H., Goswami, B. N., Vinayachandran, P. N., & Yamagata, T. (1999). A dipole mode in the tropical Indian Ocean. *Nature*, *401*, 360–363. https://doi.org/10.1038/43854

Smith, C. A., & Sardeshmukh, P. D. (2000). The effect of ENSO on the intraseasonal variance of surface temperatures in winter. *International Journal of Climatology*, *20*, 1543–1557. https://doi.org/10.1002/1097-0088(20001115)20:13<1543::aid-joc579>3.0.co;2-a

Stein, A. F., Draxler, R. R., Rolph, G. D., Stunder, B. J. B., & Cohen, M. D. (2016). NOAA's HYSPLIT atmospheric transport and dispersion modeling system. *Bulletin of the American Meteorological Society*, *96*. https://doi.org/10.1175/bams-d-14-00110.1

Stohl, A. (1998). Computation, accuracy and applications of trajectories—A review and bibliography. *Atmospheric Environment*, *32*, 947–966. https://doi.org/10.1016/s1352-2310(97)00457-3

Tamarin-Brodsky, T., Hodges, K., Hoskins, B. J., & Shepherd, T. G. (2019). A dynamical perspective on atmospheric temperature variability and its response to climate change. *Journal of Climate*, *32*, 1707–1724. https://doi.org/10.1175/jcli-d-18-0462.1

Tamarin-Brodsky, T., Hodges, K., Hoskins, B. J., & Shepherd, T. G. (2020). Changes in Northern Hemisphere temperature variability shaped by regional warming patterns. *Nature Geoscience*, *13*, 414–421. https://doi.org/10.1038/s41561-020-0576-3

Thompson, D. W. J., & Wallace, J. M. (2001). Regional climate impacts of the Northern Hemisphere annular mode. *Science*, *293*, 85–89. https://doi.org/10.1126/science.1058958

Wallace, J. M., & Gutzler, D. S. (1981). Teleconnections in the geopotential height field during the Northern Hemisphere winter. *Monthly Weather Review*, *109*, 784–812. https://doi.org/10.1175/1520-0493(1981)109<0784:titghf>2.0.co;2

Walther, G.-R., Post, E., Convey, P., Menzel, A., Parmesan, C., Beebee, T. J. C., et al. (2002). Ecological responses to recent climate change. *Nature*, *416*, 389–395. https://doi.org/10.1038/416389a

Whiteman, C. D., Zhong, S., Shaw, W. J., Hubbe, J. M., Bian, X., & Mittelstadt, J. (2001). Cold pools in the Columbia Basin. *Weather and Forecasting*, *16*, 432–447. https://doi.org/10.1175/1520-0434(2001)016<0432:cpitcb>2.0.co;2